Progress In Electromagnetics Research, Vol. 141, 327–346, 2013

A NEAR-FIELD 3D CIRCULAR SAR IMAGING TECHNIQUE BASED ON SPHERICAL WAVE DECOMPOSITION

Biao Zhang*, Yiming Pi, and Rui Min

School of Electronic Engineering, University of Electronic Science and Technology of China, Chengdu 611731, China

Abstract—A near-field three dimensional imaging algorithm for circular SAR is proposed in this paper. It adopts the theory of spherical wave decomposition to transform Green function to a superposition of plane wave components. Using this relation, the image-reconstruction can be implemented in frequency domain instead of in spatial domain, which simplifies the solving process of target reflectivity function, and allows for the target to be near to the radar. Through compensating phase factor and filtering at each elevation, we firstly get the ground CSAR signal of each elevation in frequency domain. Then, performing two dimensional inverse nonuniform fast Fourier transform and accumulating the results of all azimuth angles, the reconstructed two dimensional image corresponding to an elevation is achieved. Finally, using reconstructed image datum of all elevation, the three dimensional image of target is obtained. To demonstrate the imaging performance of our method, numerical simulations and experiments are conducted. By comparing the results with the focusing operator algorithm and the back-projection algorithm, it is found that the proposed algorithm is more efficient and can obtain a good imaging performance.

1. INTRODUCTION

With the increasing threat of terrorism, it is important and necessary to detect the concealed dangerous objects at security checkpoints such as airports, subways and train stations. At present, traditional means for detecting the concealed objects at high-security checkpoints is metal detector for personnel. However, this system has two shortcomings:

Received 20 May 2013, Accepted 6 July 2013, Scheduled 22 July 2013

* Corresponding author: Biao Zhang (zhangbiao_01@163.com).

1. Detecting results may include false detection for metal innocuous objects in personnel, such as glasses, belt buckles, keys etc.; 2. It is incapable to detect dangerous items which are made of innovative materials, such as ceramic pistols and liquid explosives [1–3]. To overcome drawbacks of metal detectors, microwave imaging systems are paid more and more attention. They benefit from two advantages: firstly, some high frequency electromagnetic waves, such as millimeter waves (MMW) and terahertz waves (THz) can penetrate clothing or packages; secondly, microwaves are nonionizing and, therefore, microwave imaging systems are easily accepted by the public. These merits make microwave imaging systems have great potential in the field of concealed objects detection [4–8]. Besides detecting concealed objects in security check, microwave near-field imaging is also applied to non-destructive testing for quality compliance industrial procedures, images acquisition of vivo tissues for biological and medical studies and far-field radar cross-section (RCS) prediction with near-field measurement of target back-scattering properties [9–12]. So, the microwave near-field imaging has become an attractive topic.

Synthetic aperture radar (SAR) is the main means of microwave imaging and many aperture synthetic modes have been proposed [13–16]. Circular SAR (CSAR) is a special aperture synthetic mode [12, 16–18]. In this mode, the target is illuminated by radar over a circular trajectory. Comparing with linear SAR (LSAR), this special mode enables CSAR achieves higher resolution, all-directional observation and three dimensional imaging. Because of these attractive features, CSAR has raised the interests of many researchers. However, because of the special rotation motion trail of CSAR, traditional algorithms for LSAR such as range Doppler (RD) algorithm, chirp scaling (CS) algorithm, and range migration algorithm (RMA) cannot be used to process CSAR data. In addition, the curved wavefronts cannot be neglected under the near-field condition. And the conventional algorithms based on the assumption of the plane wave cannot be used directly, because this approximation results in the phase deviation of the radar echo and severely limits the resolution of the near-field imaging system.

For processing near-field CSAR data, a common way is back-projection (BP) algorithm which is an extension of the computed tomography (CT) imaging in medicine [4, 19]. In this algorithm, by calculating the distance from each radar azimuth to each scatterer in the scene, we can obtain the echo of each scatterer in different azimuth through any interpolation scheme. Then, the three dimensional (3D) image of the target is achieved by accumulate these echoes of each scatterer. Although it can work with arbitrary geometry, the

computation of BP algorithm is inefficient due to the interpolation operation.

Another method for processing CSAR data is the focusing operator (FO) algorithm which uses the focusing operator to compensate the altitude and the phase variations along the wave propagation path [4, 19, 20]. Due to the phase compensation operation for all pixels in scene, this algorithm has even lower computational efficiency than BP algorithm.

To overcome the computational inefficiency of the above algorithms, Soumekh has developed a fast algorithm which is based on the Fourier analysis for the Green's function [21, 22]. In this algorithm, the generalized Parseval's theorem is used to transform the SAR echoes from the spatial domain to the spatial frequency domain. Then, the CSAR data of slant plane are transformed to ground plane by pseudo-inverse operation. Finally, the transformed data will be used in the ground plane CSAR reconstruction to obtain the target function. Due to processing radar echoes in spatial frequency domain, this algorithm improves the calculation efficiency greatly. However, the step of taking pseudo-inverse to convert the slant plane data to ground plane data may cause instability. To improve error bounds and instability caused by pseudo-inverse, Burki and Barnes propose Householder transform algorithm, but this algorithm increases the complexity and computational load [23].

In Ref. [24], a reconstruction algorithm of ω-k type which suits for wideband CSAR data taken in stripmap mode is presented. The algorithm allows to reconstruct a two dimensional (2D) image on a cylindrical surface and the range trajectory is approximated by Taylor Series expansion using only the quadratic terms. However, the angular reconstruction area and the length of the circular aperture for a single scatterer are restricted by this range approximation. To overcome these disadvantages, an improved algorithm of ω-k is proposed [25]. These two algorithms only reconstruct a 2D image. A 3D image is achieved by repeating this 2D reconstructing algorithm on different cylindrical surfaces.

More recently, a 3D near-field CSAR imaging algorithm for the system in which the receiver is a linear array of receiving elements has been proposed by Olivadese et al. [26]. In this algorithm, the wavefront curvature is taken into account by using a planar piecewise approximation. But, this approximation may limit the resolution of the near-field imaging system. In Ref. [12], an imaging algorithm for 3D near-field target reconstruction with multiple-pass CSAR observations is presented. Due to processing the radar echo in frequency domain, this method can fast reconstruct the 3D target image. Nevertheless,

this algorithm only suits for this special aperture mode and it is difficult for the real time detection of concealed weapons in practice, because the system needs to scan the target in different elevation passes.

In this paper, we propose a 3D near-field imaging algorithm for CSAR which is based on spherical wave decomposition theory. In this algorithm, the Green's function can be transformed into a superposition of plane wave components by using spherical wave decomposition theory. Therefore, the target spread function is transformed from spatial domain to spatial frequency domain. Then, the height phase term is compensated in the spatial frequency domain. Finally, the target function can be obtained by using 2D inverse nonuniform fast Fourier transform (NUFFT) and summing all azimuth results. Comparing the numerical simulation and experiment results with FO algorithm and BP algorithm, the performance of the proposed algorithm is verified. The imaging technique developed in this paper does not have the Fresnel approximation, so it can be used to reconstruct the near-field image of the target. This is because the spherical wavefronts in the near-field of the target are decomposed into plane-wave components using the spherical wave decomposition theory. The proposed method for the CSAR near-field imaging can be used in the 3D automatic target recognition (ATR) in anechoic chamber, near-field RCS measurement, detection of concealed weapons and so on.

The outline of the paper is organized as follows. Section 2 presents the CSAR imaging geometry, near-field target scattering signal model and the derivation and processing steps of the proposed algorithm. Section 3 gives the resolution and sampling criteria. Section 4 assesses the performance of this algorithm by means of numerical results. Section 5 gives the turntable experiment imaging results achieved by our proposed algorithm. Finally, the conclusions of this paper are provided in Section 6.

2. SYSTEM MODEL

The geometry of CSAR near-field imaging system is shown in Fig. 1. A radar sensor moves along a circular path with radius R_g on the plane $z = H$. As the sensor moves, its beam center always points at the center of the scene which is the origin O of the spatial coordinates (x, y, z) with the incident angle θ_i. In Cartesian coordinate system, the coordinates of the radar in the spatial domain is expressed as

$$\vec{r}_s = \left(x', y', z'\right) = (R_g \cos\theta, R_g \sin\theta, H) \tag{1}$$

where $\theta \in [0, 2\pi)$ represents slow time or aspect angle synthetic aperture domain.

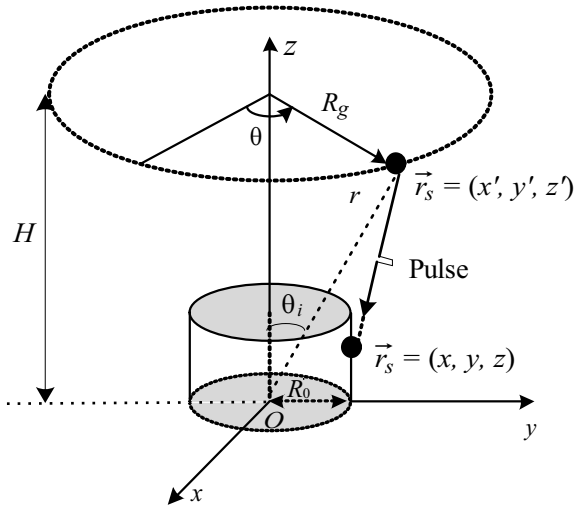

Figure 1. Geometry of the imaging system.

Supposing that there is an arbitrary point located at $\vec{r} = (x, y, z)$. Thus, the instantaneous distance from radar sensor to this point is determined by

$$\begin{aligned} R &= |\vec{r}_s - \vec{r}| = \sqrt{(x' - x)^2 + (y' - y)^2 + (z' - z)^2} \\ &= \sqrt{(x' - x)^2 + (y' - y)^2 + H_z^2} \end{aligned} \tag{2}$$

where $H_z = z' - z$.

2.1. Near-field Scattering Signal Model

The field radiated by an antenna or scattered by an object is usually subdivided into three regions: (a) reactive near-field, (b) radiating near-field (Fresnel) and (c) far-field (Fraunhofer) regions. The regions of (b) and (c) are radiation field. In these two regions, electric and magnetic field components to each other are orthogonal and wave impendence is constant. Therefore, the radial field component can be appreciable [27].

Supposing that the radar is located in the near-field (Fresnel) zone of the objects and the amplitude attenuation of the scattering field is negligible compared to the phase contribution, the echo of the target in the near-field can be expressed as [21].

$$s(k, \theta) = \iint f\left[x, y, z(x, y)\right] e^{-j2kR} dxdy \tag{3}$$

where $f[x, y, z(x, y)]$ represents the target function of a single scatterer at (x, y) with altitude $z(x, y)$, $k = 2\pi f/c$ is the wavenumber, $k \in [k_{\min}, k_{\max}]$, f is the signal frequency, c is the speed of light. The exponential term in (3) represents a spherical wave emanating from (x', y', z'), which can be decomposed into a superposition of plane wave components [1]

$$\begin{aligned} e^{-j2kR} &= e^{-j2k\sqrt{(x'-x)^2+(y'-y)^2+(z'-z)^2}} \\ &= \iint e^{jk_{x'}(x'-x)+jk_{y'}(y'-y)+jk_{z'}H_z} dk_{x'}k_{y'} \end{aligned} \tag{4}$$

where $k_{x'}$ and $k_{y'}$ are the Fourier-transform variables corresponding to x' and y', respectively. They have the following forms:

$$\begin{aligned} k_{x'} &= \frac{\partial \varphi}{\partial x'} = -2k\frac{x'-x}{R} \\ k_{y'} &= \frac{\partial \varphi}{\partial y'} = -2k\frac{y'-y}{R}. \end{aligned} \tag{5}$$

Thus, the instantaneous wave number with respect to spatial variable z' can be expressed as

$$k_{z'} = -\sqrt{4k^2 - k_{x'}^2 - k_{y'}^2} \tag{6}$$

2.2. Near-field Target Reconstruction

Target reconstruction is the solving process of target function from radar echoes, i.e., the extraction process of $f(x, y, z)$ from $s(k, \theta)$ in (3). Because the form of (3) resembles the Fourier transform, the target function can be obtained by using an integral resembling its inverse transform with respect to k and θ, i.e., [19, 20]

$$f(x, y, z) = \iint ks(k, \theta)e^{j2kR} dk d\theta \tag{7}$$

Because the single integral with respect to k in (7) can be regarded as the inverse Fourier transform of a function $ks(k, \theta)$, [4] uses the back-projection method to solve this double integral. In [19], the integral operator ke^{j2kR} in (7) is used as the focusing function to compensate for the phase of each target point.

In this paper, we use the theory of spherical wave decomposition to transform the exponential term e^{j2kR} in (7) to the superposition of plane-wave components. This exponential term is the complex conjugate of (4), i.e.,

$$\begin{aligned} e^{j2kR} &= e^{j2k\sqrt{(x'-x)^2+(y'-y)^2+(z'-z)^2}} \\ &= \iint e^{-jk_{x'}(x'-x)-jk_{y'}(y'-y)-jk_{z'}H_z} dk_{x'}k_{y'} \end{aligned} \tag{8}$$

By putting (8) in (7), (7) becomes

$$f(x,y,z) = \iint \left[\iint ks(k,\theta) e^{jk_{x'}(x-x')+jk_{y'}(y-y')-jk_{z'}H_z} dk_{x'} dk_{y'} \right] dk d\theta. \quad (9)$$

Because the coordinate systems of radar and target are coincident, the distinction between the primed and unprimed coordinate systems is dropped and the (7) is expressed as

$$f(x,y,z) = \int \left\{ \iint \left[\int ks(k,\theta) e^{-j(k_x x'+k_y y')} e^{-jk_z H_z} dk \right] e^{jk_x x+jk_y y} dk_x dk_y \right\} d\theta. \quad (10)$$

It is seen that the bracketed integral is the 2D Fourier transform result of a scatterer's reflectivity at an azimuth and can be expressed as

$$G(\theta, k_x, k_y) = \int_k Q(k,\theta,k_x,k_y) e^{-jk_z H_z} dk \quad (11)$$

where

$$Q(k,\theta,k_x,k_y) = ks(k,\theta) e^{-j(k_x x'+k_y y')} \quad (12)$$

The exponential term in (11) is the phase compensation term which compensates the phase interference caused by near-field spherical wave. Through this compensation, the images of all targets in the given plane are focused. Figs. 2(a) and (b) show the results of uncompensated phase and compensated phase.

Since the (11) is the polar spectrum of the target in $k_x - k_y$ domain and does not have the form of the rectangular spectrum, the 2D inverse Fourier transform cannot be directly performed for this spectrum. A generally method to solve this problem is the linear interpolation, but this decreases the computational efficiency. Here, the NUFFT approach is used to accurately evaluate the integrals within the braces. Due to the double integral in the braces is 2D inverse Fourier transform, the NUFFT based on min-max approach is applied [28].

Then, accumulating the 2-D inverse NUFFT result at each azimuth, we can obtain the desired image of a scatterer at the given elevation z. This process can be expressed as

$$f(x,y,z) = \int F^{-1}_{k_x,k_y}[G(\theta,k_x,k_y)] d\theta \quad (13)$$

where $F^{-1}_{k_x,k_y}$ indicates the 2D inverse FFT with respect to k_x and k_y.

To form the final 3D image of the target, we need to reconstruct the image at equally spaced elevations.

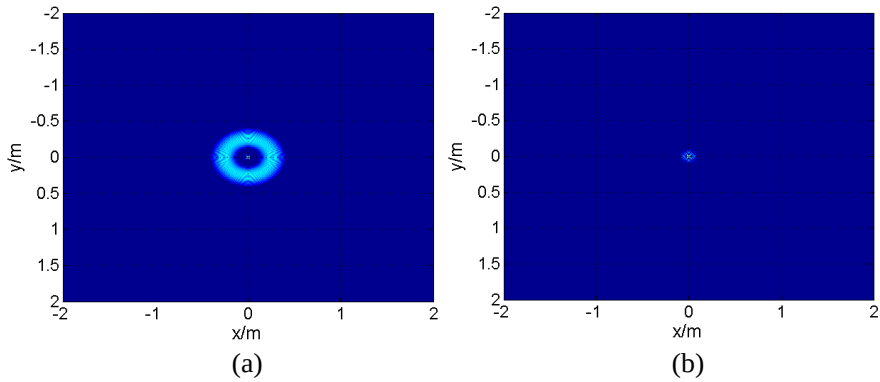

Figure 2. Image results of a scatterer within uncompensated phase and compensated phase: (a) Uncompensated phase, (b) compensated phase.

2.3. Reconstruction Procedure

This section deals with the practical implementation of spherical wave 3D reconstruction algorithm. The whole procedure to reconstruct the 3D image of a target is summarized in the flowchart in Fig. 3 and the major processing steps are listed as follows.

Step 1: Perform the phase compensation of $Q(k, \theta, k_x, k_y)$ according to (11) and obtain the frequency spectrum data $G(\theta, k_x, k_y)$ of a scatterer at a given elevation z.

Step 2: Use the inverse NUFFT method to obtain the result of a target at an azimuth angle and a given elevation.

Step 3: Coherent summation over all azimuth angles to obtain a 2D image result of targets at a given elevation.

Step 4: Repeating Step 1 to Step 3 for each elevation, the 3D image of a target is obtained.

3. SAMPLING CRITERIA AND RESOLUTION

3.1. Resolutions

Assuming that a single scatterer placed at the origin is an omnidirective reflector, i.e., radar can receive the echo of this scatterer at all direction, the range and azimuth resolutions in CSAR mode depend on the mainlobe of point spread function (PSF) and this function has the

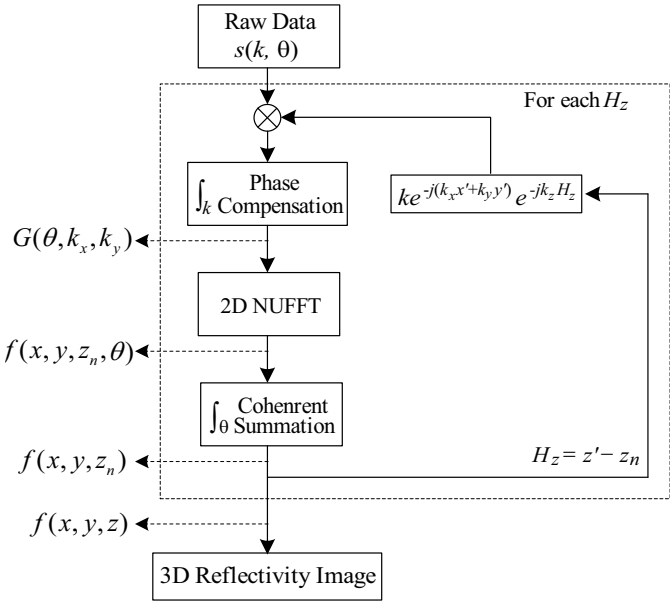

Figure 3. Flowchart of near-field 3D imaging algorithm for CSAR.

expression of

$$\mathrm{PSF}(x,y) = \rho_{\max}\frac{J_1(r_0\rho_{\max})}{r_0} - \rho_{\min}\frac{J_1(r_0\rho_{\min})}{r_0} \tag{14}$$

where $r_0 = \sqrt{x^2+y^2}$, J_1 is the Bessel function of the first kind, first order and

$$\begin{aligned}\rho_{\max} &= 2k_{\max}\sin\theta_i \\ \rho_{\min} &= 2k_{\min}\sin\theta_i\end{aligned} \tag{15}$$

where $k_{\min}$ and $k_{\max}$ are minimum wavenumber and maximum wavenumber of transmitted signal [21]. Generally, the resolution of an image is estimated by the mainlobe width of PSF [29]. Here, we consider the 3 dB mainlobe width of PSF as the corresponding range and cross-range resolutions:

$$\Delta x = \Delta y \approx \frac{2.4}{2k_c\sin\theta_i} \tag{16}$$

where k_c is the wavenumber at carrier frequency.

The elevation resolution is approximately

$$\Delta z \approx \frac{2c}{\sqrt{2\pi}B\cos\theta_i} \tag{17}$$

where c is the light speed and B is the signal bandwidth.

3.2. Sampling Criteria

From the Nyquist sampling theorem, we know that the signal sampling intervals in the range domain and azimuth domain depend on the extent of bandwidth in the corresponding frequency domain. In fast time domain, the wavenumber bandwidth of the transmitted signal is

$$\Omega_k = [2k_{\min}, 2k_{\max}]. \tag{18}$$

Therefore, the sampling frequency in the fast time domain is determined by

$$\Delta f \leq \frac{c}{2R_{\max}} \tag{19}$$

where Δf is the frequency sampling interval and $R_{\max}$ represents the maximum detectable distance.

The maximum support of the CSAR signal spectrum in the slow time frequency domain is

$$\Omega_\theta = [-2k_{\max} \sin\theta_i, 2k_{\max} \sin\theta_i] \tag{20}$$

Thus, the sampling interval in slow time domain should satisfy the following:

$$\Delta\theta \leq \frac{\pi}{2k_{\max} \sin\theta_i R_0} \tag{21}$$

Equation (21) indicates that the slow time sampling interval decreases with the increase of the incident angle, signal frequency and the scene size.

4. SIMULATION RESULTS

In this section, two simulation experiments are used to validate performance of the proposed algorithm. In the first simulation, the resolution and sidelobe metrics of the proposed algorithm are analyzed. The PSFs of three reconstruction algorithms are compared to demonstrate the performance of the proposed method. In the second simulation, the 3D image reconstruction capability of the proposed algorithm is verified.

In CSAR mode, PSF is the reconstructed image of a single scatterer located at the origin of the coordinate system. The 3 dB width of its mainlobe represents the resolution of a reconstructed image and this function can be also used to evaluate the sidelobe metric. Thus, the performance of the proposed algorithm is examined through its PSF. The main system simulation parameters appear in Table 1.

The PSF images obtained via the FO algorithm, BP algorithm and our method are shown in Fig. 4, respectively. Comparing three images

Table 1. System simulation parameters.

Parameter	Value
Carrier frequency f_c	9.6 GHz
Bandwidth B	660 MHz
Range sampling number N_r	221
Azimuth sampling number N_a	3600
Slant range R_c	8 m
Scene Radius R_0	2 m
Incident angle θ_i	70°

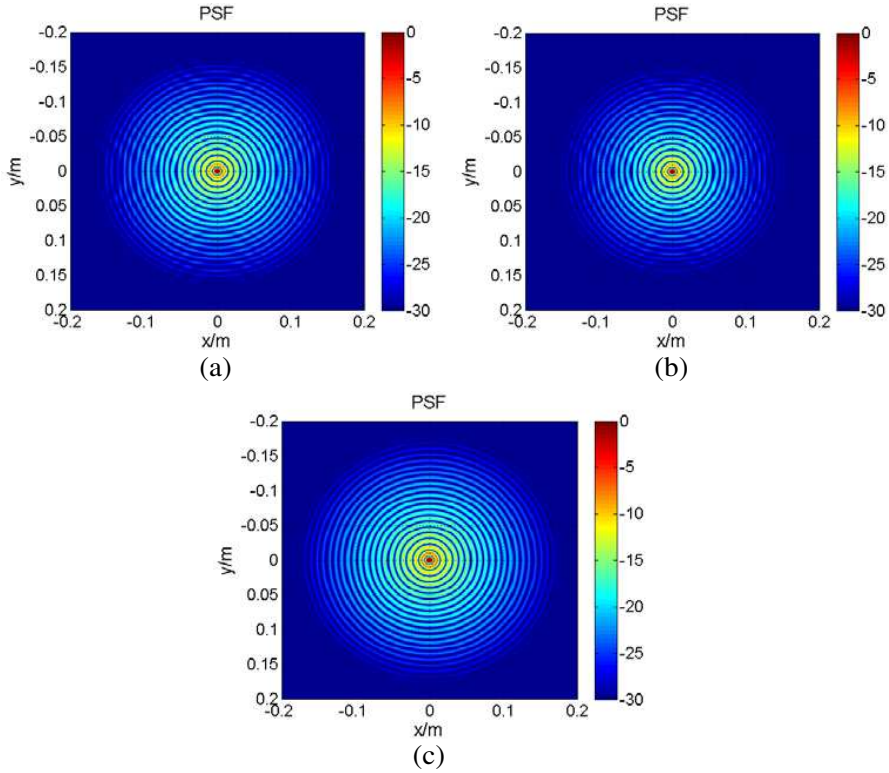

Figure 4. PSF images of three algorithms: (a) FO algorithm, (b) BP algorithm, (c) our method.

in Fig. 4, the −30 dB PSF image areas of the BP algorithm and FO method are lower than the proposed algorithm. But, the PSF image of our method is more ideal than the other two algorithms, because the reconstructed image of the proposed algorithm has perfect concentric circles.

Table 2. Image performance parameters.

Algorithm	PSLR (dB)	X-Y Resolution (mm)	Processing Time (s)
FO	−8.4	6.45	8329.5
BP	−8.0	6.49	341.8
Our method	−8.0	6.47	12.2

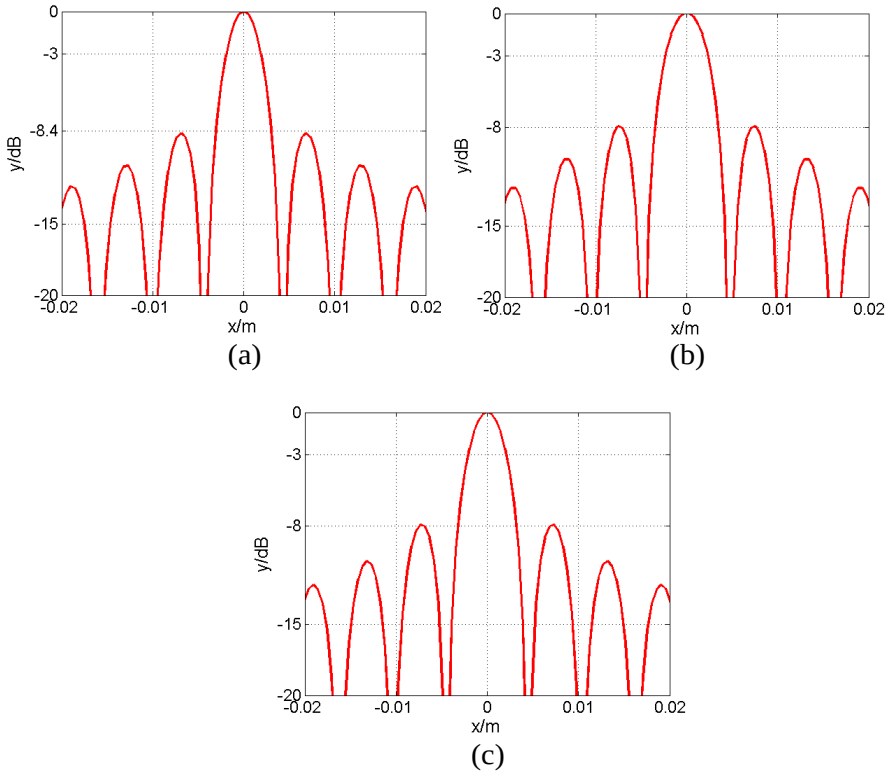

Figure 5. PSLR and mainlobe width of the three algorithms: (a) FO algorithm, (b) BP algorithm, (c) our method.

In order to quantitatively analyze the performance of the proposed algorithm, the resolution, the peak sidelobe rate (PSLR) and cost time are evaluated in Table 2. The PSLR is the ratio between the peak value of the largest sidelobe A_{side} and the peak value of the mainlobe A_{main} and it is expressed as

$$\mathrm{PSLR} = 20\log_{10}\left[\frac{A_{side}}{A_{main}}\right]. \tag{22}$$

The PSLR and -3 dB mainlobe width of the PSF images, which are reconstructed by the three algorithms respectively are in Fig. 5.

From Fig. 5 and Table 2, we can see that the proposed algorithm has a close accuracy to BP. Although the sidelobe level of our method is higher than the FO, our method is more efficient in processing CSAR data.

To validate the 3D image reconstruction feasibility of the proposed algorithm, the 3D geometry structure formed by 9 scatterers with reflectivity value 1 is used in the simulation. The parameters used in this simulation experiment are listed in Table 1. From the Fig. 6(a), we can see that the target extension dimension D is about 2.8 m. According to the far field requirement $R \geq 2D^2/\lambda$, the target far field range is equal or greater than 519 m. In our simulation experiment, the range from radar to target is only 8 m, so the radar is in the near-field zone of the target.

The 3D imaging result obtained via proposed algorithm is shown in Fig. 6(b). It can be seen that 9 scatterers in different planes are focused very well. The position of each reconstructed point is nearly consistent with its actual position. And the reconstructed image is consistent with the 3D simulation geometrical structure. Figs. 6(c)–(e) show 2D image of scatterers in each plane, and the dynamic range of each image is 25 dB. Comparing these images, we also find that the reconstructed points at $z = 0$ are smaller than those at $z = 1$ and $z = -1$. The reason for this phenomenon is that the resolution of a scatterer in scene declines with range to the scene center.

5. EXPERIMENT RESULTS

In this section, the turntable data of the T72 tank collected by the group at Georgia Tech Research Institute (GTRI) in the United States are used to provide experimental validation to the proposed method. The turntable SAR parameters are shown in Table 3.

As shown in the table, the maximum frequency of the SAR system is 9.93 GHz and the target extension dimension D is about 9.4 m, and the distance between radar to the center of turntable is 52.88 m.

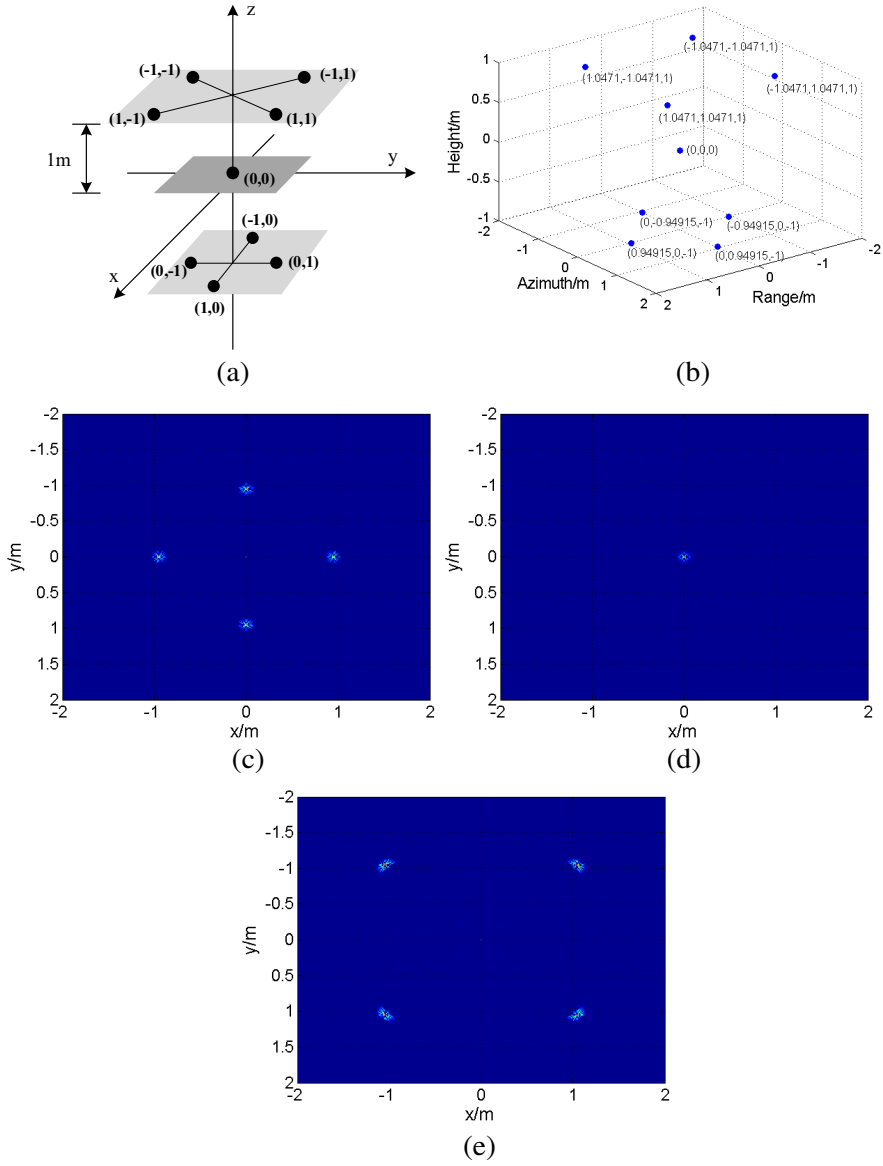

Figure 6. Simulation results: (a) 3D scatterers structure, (b) 3D reconstructed image, (c) slice image at $z = -1\,\mathrm{m}$, (d) slice image at $z = 0\,\mathrm{m}$, (e) slice image at $z = 1\,\mathrm{m}$.

Table 3. System simulation parameters.

Parameter	Value
Carrier frequency f_c	9.6 GHz
Bandwidth B	660 MHz
Range sampling number N_r	221
Azimuth sampling number N_a	6715
Slant range R_c	52.88 m
Scene Radius R_0	7.2 m
Incident angle θ_i	60°

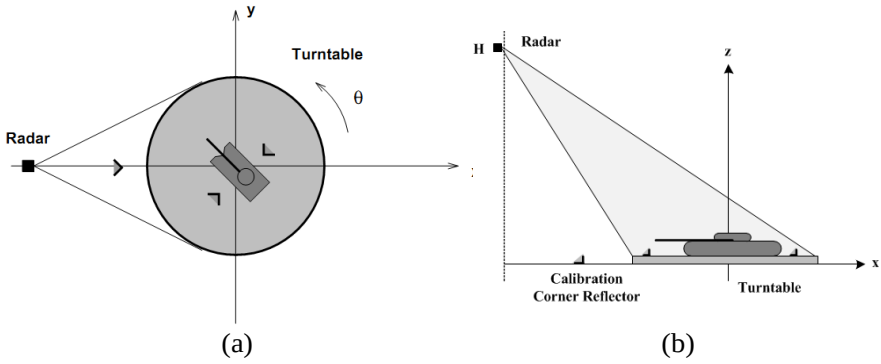

Figure 7. Turntable imaging geometry: (a) Top view, (b) side view.

According to the far-field criteria, the far-field range of the target should be equal or greater than 5849.4 m. Therefore, the target is in the near-field zone and this turntable SAR data meet the requirement of the near-field imaging. Figs. 7(a) and (b) show the turntable imaging geometry [30].

Figures 8(a)–(f) show six slices of the tank 3D image at $z = -2$, -1.25, 0, 0.75, 1.25 and 2 m. As shown in Fig. 8, different parts of the T72 tank are focused in different elevation z. For example, the two corner reflectors are focused very well at $z = -1.25$ m, the focused barrel appears at $z = 0.75$ m and the tank turret is focused at $z = 2$ m.

The imaging results in Figs. 9(a)–(c) are 2D images at the elevation $z = 0$ m reconstructed by FO algorithm, BP algorithm and our proposed method. To reconstruct this 2D image, our method costs only about 13 seconds. The other two algorithms need about hundreds or even thousands of seconds for reconstruct an image. The

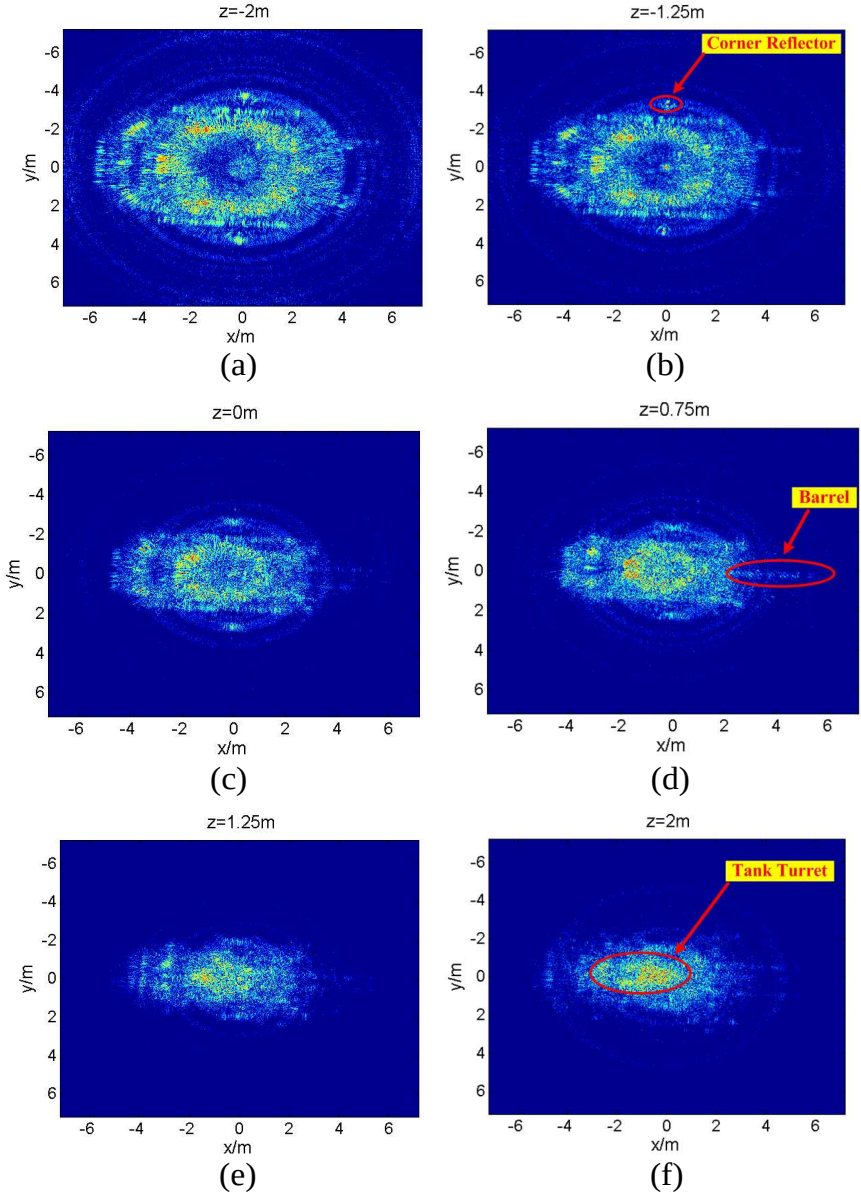

Figure 8. T72 tank 3D image: (a) Image result at $z = -2\,\mathrm{m}$, (b) image result at $z = -1.25\,\mathrm{m}$, (c) image result at $z = 0\,\mathrm{m}$, (d) image result at $z = 0.75\,\mathrm{m}$, (e) image result at $z = 1.25\,\mathrm{m}$, (f) image result at $z = 2\,\mathrm{m}$.

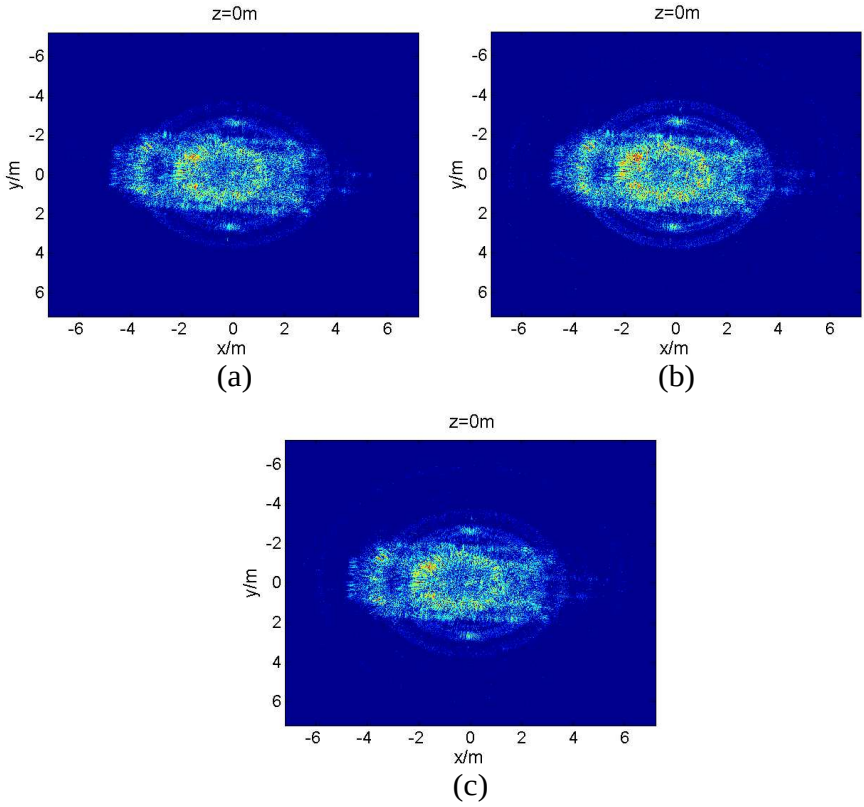

Figure 9. Imaging results of a slice at $z = 0$: (a) FO algorithm, (b) BP algorithm, (c) our method.

comparison of these results shows that the proposed algorithm has the same accuracy but needs less processing time. Therefore, the proposed algorithm in this paper has potential prospect in the real time detection and imaging field.

6. CONCLUSIONS

In this paper, we propose a near-field 3D imaging algorithm for CSAR which is based on the theory of the spherical wave decomposition. By using this theory, the Green's function is transformed to a superposition of plane wave components and the far-field assumption is not used in this transformation process. Therefore, this algorithm can be used to reconstruct an image of the target in the near-field

zone. The PSF images, resolutions, sidelobe levels and computational time of the FO algorithm, BP algorithm and the proposed method are discussed in details. Compared with the other two algorithms, this algorithm overcomes the problem of the computational inefficiency and achieves a good performance. The simulation and experiment results validate the effectiveness of the proposed algorithm for the 3D target reconstruction.

ACKNOWLEDGMENT

The authors would like to thank the anonymous reviewers for providing a number of important comments and suggestions. The work described in this paper is supported by the National Natural Science Foundation of China (Grant No. 61271287).

REFERENCES

1. Sheen, D. M., D. L. McMakin, and T. E. Hall, "Three-dimensional millimeter-wave imaging for concealed weapon detection," *IEEE Trans. on Microwave Theory and Techniques*, Vol. 49, No. 9, 1581–1592, Sep. 2001.
2. Sheen, D. M., D. L. McMakin, and T. E. Hall, "Near-field three-dimensional radar imaging techniques and applications," *Applied Optics*, Vol. 49, No. 19, E83–E93, 2010.
3. Oka, S., H. Togo, N. Kukutsu, and T. Nagatsuma, "Latest trends in millimeter-wave imaging technology," *Progress In Electromagnetics Research Letters*, Vol. 1, 197–204, 2008.
4. Demirci, S., H. Cetinkaya, E. Yigit, C. Ozdemir, and A. Vertiy, "A study on millimeter-wave imaging of concealed objected: Application using back-projection algorithm," *Progress In Electromagnetics Research*, Vol. 128, 457–477, 2012.
5. Manfred, H., B. Gunnar, and E. Helmut, "Millimetre wave near-field SAR scanner for concealed weapon detection," *Proceedings of EUSAR 2008*, 151–154, Friedrichshafen, Germany, 2008.
6. Harmer, S. W., S. E. Cole, N. J. Bowring, N. D. Rezgui, and D. Andrews, "On body concealed weapon detection using a phased antenna array," *Progress In Electromagnetics Research*, Vol. 124, 187–210, 2012.
7. Grokhotkov, I. N. and A. Kuznetsov, "A concept of microwave system for the inspection of people and luggage," *Proceedings of EUSAR 2008*, 155–159, Friedrichshafen, Germany, 2008.

8. Bjarnason, J. E., T. L. Chan, A. W. Lee, M. A. Celis, and E. R. Brown, "Millimeter-wave, terahertz, and mid-infrared transmission through common clothing," *Applied Physics Letters*, Vol. 85, No. 4, 197–204, 2004.
9. Tonouchi, M., "Cutting-edge terahertz technology," *Nature Photonics*, Vol. 1, No. 2, 97–105, 2007.
10. Li, J. and Y. Pi, "Research on the 3D imaging algorithm of spin target based on the Hough transform," *EURASIP Journal on Wireless Communications and Networking*, Vol. 90, 2013, doi:10.1186/1687-1499-2013-90.
11. Nicholson, K. J. and C. H. Wang, "Improved near-field radar cross-section measurement technique," *IEEE Antennas and Wireless Propagation Letters*, Vol. 8, 1103–1106, 2009.
12. Yan, W., J.-D. Xu, N.-J. Li, and W.-X. Tan, "A novel fast near-field electromagnetic imaging method for full rotation problem," *Progress In Electromagnetics Research*, Vol. 120, 387–401, 2011.
13. Li, C. and D. Y. Zhu, "A residue-pairing algorithm for InSAR phase unwrapping," *Progress In Electromagnetics Research*, Vol. 95, 341–354, 2009.
14. Ren, X. Z., L. H. Qiao, and Y. Qin, "A three-dimensional imaging algorithm for tomography SAR based on improved interpolated array transform," *Progress In Electromagnetics Research*, Vol. 120, 181–193, 2011.
15. Xu, J., Y. Pi, and Z. Cao, "Bayesian compressive sensing in synthetic aperture radar imaging," *IET Radar Sonar Navig.*, Vol. 6, No. 1, 2–8, 2012.
16. Tan, W. X., W. Hong, Y. P. Wang, and Y. R. Wu, "A novel spherical-wave three-dimensional imaging algorithm for microwave cylindrical scanning geometries," *Progress In Electromagnetics Research*, Vol. 111, 43–70, 2011.
17. Yu, L. and Y. Zhang, "A 3D target imaging algorithm based on two-pass circular SAR observations," *Progress In Electromagnetics Research*, Vol. 122, 341–360, 2012.
18. Knaell, K. K. and G. P. Cardillo, "Radar tomography for the generation of three-dimensional images," *IEE Proc. of Radar, Sonar, Navigation*, Vol. 142, No. 2, 54–60, 1995.
19. Broquetas, A., J. Palau, L. Jofre, and A. Cardama, "Spherical wave near-field imaging and radar cross-section measurement," *IEEE Trans. Antennas Propag.*, Vol. 46, No. 5, 730–735, May 1998.
20. Broquetas, A., L. Jofre, and A. Cardama, "A near-field spherical

wave inverse synthetic aperture radar technique," *IEEE AP-S Symp. Dig.*, Vol. 2, 1114–1117, Chicago, IL, 1992.

21. Soumekh, M., *Synthetic Aperture Radar Signal Processing with MATLAB Algorithms*, Wiley, New York, 1999.
22. Soumekh, M., "Reconnaissance with slant plane circular SAR imaging," *IEEE Transactions on Image Processing*, Vol. 5, No. 8, 1252–1265, 1996.
23. Burki, J. and C. F. Barnes, "Slant plane CSAR processing using householder transform," *IEEE Transactions on Image Processing*, Vol. 17, No. 10, 1900–1907, 2008.
24. Dallinger, A., S. Schelkshorn, and J. Detlefsen, "Efficient ω-k algorithm for circular SAR and cylindrical reconstruction areas," *Advances in Radio Science*, Vol. 4, No. 10, 85–91, 2006.
25. Kou, L. L., X. Q. Wang, J. S. Chong, M. S. Xiang, and M. H. Zhu, "Circular SAR processing using an improved omega-k type algorithm," *Journal of Systems Engineering and Electronics*, Vol. 21, No. 4, 572–579, 2010.
26. Olivadese, D., E. Giusti, F. Berizzi, M. Martorella, and F. Lombardini, "Near field 3D circular SAR imaging," *3rd International Asia-Pacific Conference on Synthetic Aperture Radar (APSAR)*, 2011.
27. Balanis, C. A., *Antenna Theory Analysis and Design*, 3rd Edition, John Wiley and Sons, New York, USA, 2005.
28. Fessler, J. A. and B. P. Sutton, "Nonuniform fast fourier transforms using min-max interpolation," *IEEE Transactions on Signal Processing*, Vol. 51, No. 2, 560–574, 2003.
29. Ishimaru, A., T. K. Chan, and Y. Kuga, "An imaging technique using confocal circular synthetic aperture radar," *IEEE Transactions on Geoscience and Remote Sensing*, Vol. 36, No. 5, 1524–1530, 1998.
30. Bryant, M. L., L. L. Gostin, and M. Soumekh, "3-D E-CSAR imaging of a T-72 tank and synthesis of its SAR reconstructions," *IEEE Transactions on Aerospace and Electronic Systems*, Vol. 39, No. 1, 211–227, 2003.